Exciton-coupled coherent magnons in a 2D semiconductor

https://doi.org/10.1038/s41586-022-05024-1

Received: 27 April 2022

Accepted: 24 June 2022

Published online: 7 September 2022



Check for updates

Youn Jue Bae¹, Jue Wang¹, Allen Scheie², Junwen Xu³, Daniel G. Chica¹, Geoffrey M. Diederich^{4,5}, John Cenker⁴, Michael E. Ziebel¹, Yusong Bai¹, Haowen Ren³, Cory R. Dean⁶, Milan Delor¹, Xiaodong Xu⁴, Xavier Roy¹, Andrew D. Kent³ & Xiaoyang Zhu^{1⊠}

The recent discoveries of two-dimensional (2D) magnets¹⁻⁶ and their stacking into van der Waals structures⁷⁻¹¹ have expanded the horizon of 2D phenomena. One exciting application is to exploit coherent magnons¹² as energy-efficient information carriers in spintronics and magnonics^{13,14} or as interconnects in hybrid quantum systems¹⁵⁻¹⁷. A particular opportunity arises when a 2D magnet is also a semiconductor, as reported recently for CrSBr (refs. 18-20) and NiPS₃ (refs. 21-23) that feature both tightly bound excitons with a large oscillator strength and potentially long-lived coherent magnons owing to the bandgap and spatial confinement. Although magnons and excitons are energetically mismatched by orders of magnitude, their coupling can lead to efficient optical access to spin information. Here we report strong magnon-exciton coupling in the 2D A-type antiferromagnetic semiconductor CrSBr. Coherent magnons launched by above-gap excitation modulate the exciton energies. Time-resolved exciton sensing reveals magnons that can coherently travel beyond seven micrometres, with a coherence time of above five nanoseconds. We observe these exciton-coupled coherent magnons in both even and odd numbers of layers, with and without compensated magnetization, down to the bilayer limit. Given the versatility of van der Waals heterostructures, these coherent 2D magnons may be a basis for optically accessible spintronics, magnonics and quantum interconnects.

In this study, we chose CrSBr because of its excellent semiconducting properties^{18,19}, and, more importantly, the observation of strong coupling of Wannier excitons in CrSBr to interlayer magnetic order²⁰. The CrSBr crystal consists of van der Waals (vdW) layers with rectangular unit cells in the plane (a-b) and stacked along the c axis to produce an orthorhombic structure. Atomically thin flakes of CrSBr can be produced by mechanical exfoliation, where the bulk magnetic structure is maintained down to the ferromagnetic (FM) monolayer with a Curie temperature $T_C = 146 \text{ K}$ and to the antiferromagnetic (AFM) bilayer with a Néel temperature $T_N = 140 \text{ K}$ (ref. 19), which is higher than the bulk T_N of 132 K. CrSBr is also a direct-gap semiconductor down to the monolayer, with an electronic gap of 1.5 eV and an excitonic gap of 1.34 eV (ref. 18). Towards the two-dimensional (2D) limit, the material can be with or without net magnetization for odd or even numbers of layers, respectively¹⁹. The co-existence of both magnetic and semiconducting properties implies that a spin wave may coherently modulate the electronic structure, which in a 2D semiconductor, is reflected in the dominant excitonic transitions $^{24,25}.\,Such\,2D$ magnon–exciton coupling allows the launch and detection of spin waves from strong absorption, emission or reflection of light in the energy range corresponding to excitonic transitions. This is a major advantage over conventional methods to optically access magnons by (1) resonant

excitation in microwave spectroscopy based on microwave antenna and waveguides¹³. (2) magneto-optical effects based on precise detection of light polarization rotation^{12,26} or (3) symmetry changes detected in nonlinear optical spectroscopy with high-power pulsed lasers^{19,26}.

The coupling of Wannier excitons to interlayer magnetic order in CrSBr comes from the spin-dependent interlayer electron-exchange $interaction {}^{20}. Using first-order perturbation theory, we can approximate \\$ the shift in the exciton energy ($\Delta E_{\rm ex}$) owing to changes in the interlayer electron-exchange interaction as $\Delta E_{\rm ex} \propto \cos(\theta/2)^2$ where θ is the angle between the magnetic moments (M) in neighbouring layers²⁰. In the AFM state $(\theta = \pi)$, the interlayer hybridization is spin forbidden and $\Delta E_{ex} = 0$; in the FM state (θ = 0), the interlayer electron-exchange interaction is the greatest and $\Delta E_{\rm ex}$ is -20 meV (ref. 20). The dependence of $\Delta E_{\rm ex}$ on θ is the basis for exciton sensing of coherent spin waves. To probe the dynamical change in $\Delta E_{\rm ex}$, we excite CrSBr with a femtosecond laser pulse with above-gap photon energy (hv_1) , and probe the resulting spin waves with a femtosecond broadband pulse (hv_2) at a controlled distance (d) between the pump and probe spots (Fig. 1a). We identify the magnon modes from coherent oscillations in $E_{\rm ex}$, and corroborate this assignment with frequency-domain magnetic resonance spectroscopy. The long-lived coherent magnons and their strong coupling to excitons allow us to directly image coherent magnons propagating in the 2D surface plane.

Department of Chemistry, Columbia University, New York, NY, USA, 2 Neutron Scattering Division, Oak Ridge National Laboratory, Oak Ridge, TN, USA, 3 Department of Physics, New York University, New York, NY, USA. 4Department of Physics, University of Washington, Seattle, WA, USA. 5Intelligence Community Postdoctoral Research Fellowship Program, University of Washington, Seattle, WA, USA. ⁶Department of Physics and Astronomy, Columbia University, New York, NY, USA. ⁵e-mail: xyzhu@columbia.edu

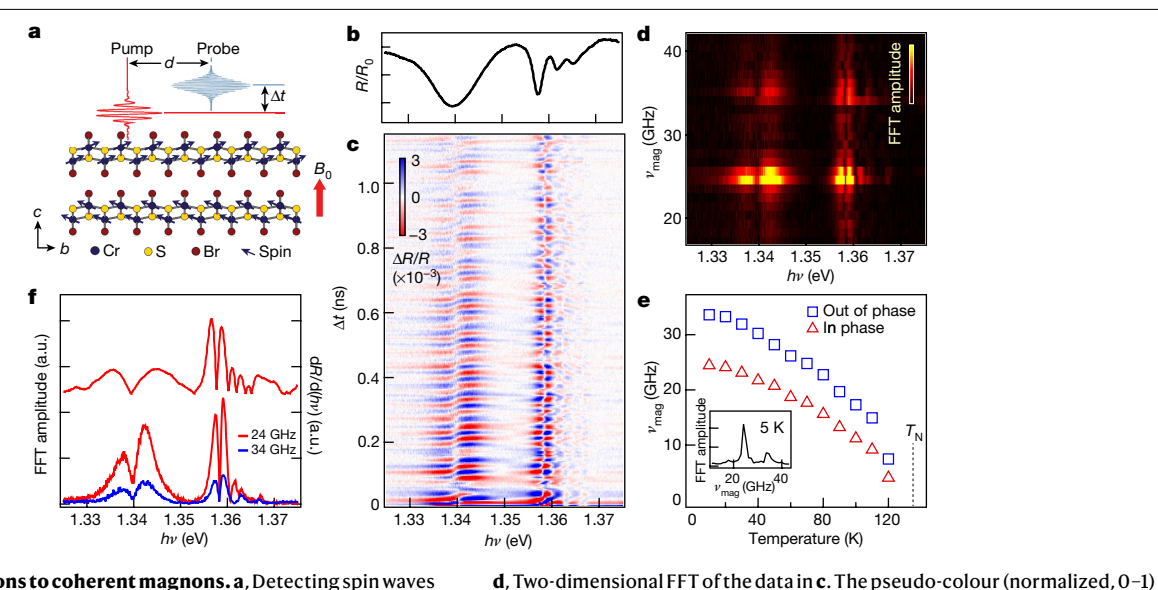


Fig. 1 | Coupling of excitons to coherent magnons. a, Detecting spin waves from transient reflectance. A femtosecond pump pulse with above-gap photon energy launches spin waves in the layered AFM semiconductor CrSBr. Reflectance from a broadband probe pulse measures coherent oscillation at excitonic transitions. An external canting field, $B_0 = 0.2$ T, is applied along the caxis (normal to the 2D planes), to enhance the oscillatory signal, **b**. Reflectance (R) from CrSBr is normalized to that of the SiO₂ substrate (R_0). c, Transient reflectance spectra $\Delta R/R$ as a function of pump-probe delay (Δt) and probe photon energy (hv). An incoherent background has been subtracted from $\Delta R/R$ (Supplementary Fig. 20). The pseudo-colour scale is $\Delta R/R$, where R is reflectance without pump and ΔR is pump-induced change in reflectance.

in **b**. All experiments are done at a sample temperature of 5 K, except **e** where the sample temperature is varied between 5 K and 140 K. The pump pulse at $hv_1 = 1.7 \text{ eV}$ (pulse width, 150 fs; repetition rate, 250 kHz; power, 1 μ W; spot diameter, 1.4 μ m) and the probe pulse at hv_2 = 1.3-1.4 eV (pulse width, about 100 fs; power, 0.2 μW; spot diameter, about 1.2 μm) are used.

is the FFT amplitude, e. The two spin-wave frequencies are shown as a function

of sample temperature below T_N . The inset is the probe $h\nu$ -integrated FFT trace

showing the two peaks at 24 GHz and 34 GHz at 5 K. f, Two horizontal cuts of the

34 GHz). Also shown is the first derivative (black) of the reflectance spectrum

2D pseudo-colour plot in d at the two peak frequencies (red. 24 GHz; blue

Magnon-exciton coupling from transient reflectance

Upon photoexcitation of CrSBr, the strong oscillatory components (Fig. 1c) come from the coherent spin waves because (1) they are observed only below T_N and the frequencies decrease with T (Supplementary Fig. 1 and Fig. 1e discussed below), and (2) the amplitude of the oscillation signal is much weaker in the absence of a canting field (Supplementary Fig. 2) and increases with an external canting field, B_0 . To obtain the frequencies of the coherent spin waves, we perform a fast Fourier transform (FFT) of the oscillatory response. Figure 1d shows the FFT amplitude (pseudo-colour) as a function of spin-wave frequency (v_{mag}) and hv_2 . There are two peak frequencies at about 24 GHz and about 34 GHz, both independent of probe hv_2 . This is expected because the coherent spin waves modulate the interlayer electronic hybridization, and thus all excitonic transitions. We use the hv₂-integrated FFT spectrum (inset of Fig. 1e for a typical spectrum at T = 5 K), to quantify the peak frequencies: $v_{\text{mag1}} = 24.6 \pm 0.7 \text{ GHz}$ and $v_{\text{mag2}} = 34 \pm 1 \text{ GHz}$. With increasing T, the magnetic order decreases and this results in lowering of the spin-wave frequencies (Fig. 1e). Around T_N , both v_{mag1} and v_{mag2} approach zero. The T dependences of v_{mag1} and v_{mag2} closely follow that of the magnetic-order parameter19.

The strong coupling of excitons to coherent magnons is revealed by clear π -phase flips of the oscillatory signal at hv_2 , corresponding exactly to the peaks of excitonic transitions (Fig. 1b,c). The π -phase shift is a signature of an optical transition modulated by coherent oscillation in a coupled mode²⁷, as is also known for coherent phonon–exciton coupling²⁸. Likewise, the FFT amplitudes of both v_{mag1} and v_{mag2} (red and blue spectra in Fig. 1f, respectively) track the first derivative (black) of the static reflectance spectrum. The strength of the coupling between excitons and coherent magnons can be calculated by the modulation of the exciton energy (detailed in Supplementary Information and Supplementary Figs. 3–5). We obtain exciton energy modulation caused by coherent magnons of $\delta E_{\rm ex} = 4.0 \pm 0.5$ meV. It is noted that this coupling is perturbative in nature, not due to resonant hybridization between two

modes that differ in energies by four orders of magnitude: $E_{\rm ex} \approx 1.3 \, {\rm eV}$ and $hv_{\text{mag}} = 0.10 \text{ meV}$ and $hv_{\text{mag}} = 0.14 \text{ meV}$ (for v_1 and v_2 , respectively).

Magnetic resonance spectroscopy

To support assignments of coherent magnon modes from excitonic sensing, we use magnetic resonance spectroscopy. Figure 2a shows a series of magnetic resonance spectra at selected microwave frequencies (v = 5-21 GHz) for bulk CrSBr at T = 5 K. The spectra reveal a single resonance in the low-frequency (≤18 GHz) region and two resonances in the high-frequency (>22 GHz) region. We extract peak frequencies (v_{mag}) of the resonances (Supplementary Fig. 6) and plot them as function of the magnetic field applied along the caxis (B_0) (Fig. 2b). For B_0 smaller than a saturation field ($B_{\text{sat}} \approx 1.7 \text{ T}$), we observe two v_{mag} branches whose frequencies decrease with increasing \boldsymbol{B}_0 , consistent with reduction in AFM order as spins are progressively canted away from the easy b axis. The frequencies of these two branches are assigned to the in-phase $(v_{\rm IP})$ and out-of-phase (v_{OP}) spin precessions, similar to those observed in the 2D AFM materials of chromium(III) chloride and chromium(III) iodide
i
-2.930. Above $B_{\rm sat}$, the spins are fully polarized parallel to
 B_0 and v_{mag} increases linearly with B_0 (seen here for the out-of-phase magnon), which is expected for a ferromagnetic resonance³¹. In agreement with the magnetic resonance results (Fig. 2b), the B_0 dependence of the excitonic transitions in transient reflectance exhibits the same dispersion for the low-frequency in-phase branch (Fig. 2c). The temperature dependence of the magnon frequencies from magnetic resonance measurements (Supplementary Fig. 7) are in good agreement with those obtained from optical measurements (Fig. 1f).

In-plane propagating coherent magnons

We exploit the efficient exciton sensing to implement time and spatially resolved spectroscopic imaging of propagating coherent magnons. We perform this with the pump and probe beam separated by a controlled

Article

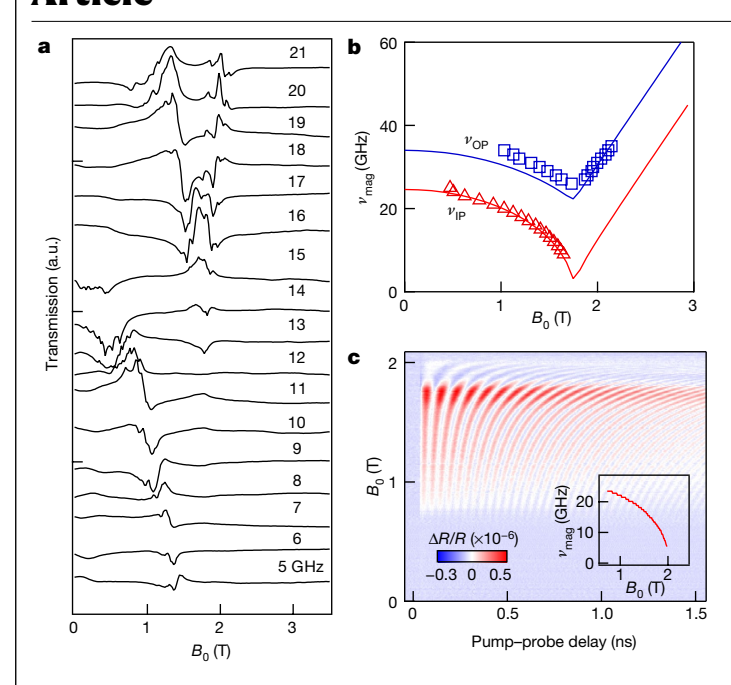


Fig. 2 | Magnetic-field-dependent magnon frequencies and calculated dispersions. a, Magnetic resonance spectra at the indicated frequencies $(5-21\,\mathrm{GHz})$ from a bulk CrSBr crystal at $T=5\,\mathrm{K}$, with the magnetic field applied along the c axis. The spectra are offset for clarity. **b**, Peak resonance frequencies as a function of magnetic field (symbols). The solid curves are dispersion fits from LSWT as detailed in Methods. **c**, Transient reflectance spectra at a single-probe wavelength with respect to the applied field along the c axis of the bulk CrSBr crystal at $5\,\mathrm{K}$. The inset shows the extracted peak frequency from the FFT spectrum as a function of magnetic field.

distance, d (Fig. 3a). The diffraction-limited excitation spot can create a gradient in the driving force for launching coherent magnons in a finite momentum window at |k| > 0. The propagating nature of the coherent magnons is clearly seen in the delayed rise of the oscillatory signal for d > 0, as illustrated for $d = 2 \mu m$ along the a axis (Fig. 3b; see Supplementary Fig. 8 for probe photon-energy-resolved propagation images). This delayed response is in stark contrast to the prompt rise of the magnon signature when the pump and probe pulses overlap spatially (d = 0) in Fig. 1c. FFT analysis of the propagating waves reveals the two coherent magnons at 24 GHz and 34 GHz. Along the a axis, we detect two magnon frequencies (24 GHz and 34 GHz); along the b axis, we detect only the 24-GHz component. We perform short-time Fourier transform (STFT) with respect to Δt for different d values for the 24-GHz and 34-GHz modes along the a axis (Fig. 3c-e) and for the 24-GHz mode along the baxis (Fig. 3d). In each case, the peak Δt shifts linearly with d, establishing the propagating nature of these coherent waves. From these shifts, we obtain group velocities of $V_{\sigma} = 1.0 \pm 0.1 \,\mathrm{km \, s^{-1}}$ and $V_{\sigma} = 3.0 \pm 0.3 \,\mathrm{km \, s^{-1}}$, for the 24-GHz and 34-GHz modes along the a axis, respectively, and $V_g = 0.7 \pm 0.1 \,\mathrm{km \, s^{-1}}$ for the 24-GHz mode along the b axis (Supplementary Fig. 9). From the probe-distance-dependent measurements along the baxis (Supplementary Fig. 8), we obtain lower bounds for the coherent transport lengths of $\lambda_{\rm coh}$ = 6 μ m and $\lambda_{\rm coh}$ = 7 μ m for the 24-GHz and 34-GHz modes, respectively. In complementary experiments, we carry out time-resolved imaging based on the magneto-optical Kerr effect (MOKE). Following initial excitation in the centre of the image frame, the MOKE responses expand in space with Δt , as expected from the propagating nature of the spin waves (detailed in Supplementary Section 2). Figure 3f shows a representative early time ($\Delta t = 0.1 \text{ ns}$) MOKE image, which is discussed below.

To understand the origin of propagating spin waves, we calculated magnon dispersions along high-symmetry directions (Fig. 4a,b) from linear spin-wave theory (LSWT) fits to neutron-scattering data³²,

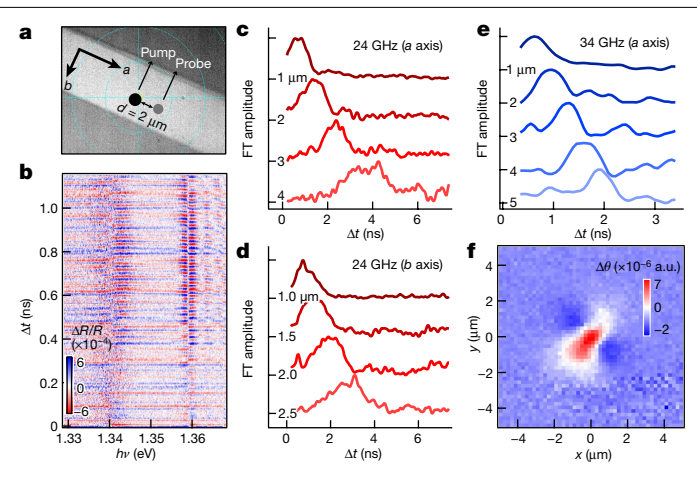


Fig. 3 | **Exciton sensing of propagating coherent AFM spin waves in the 2D plane. a**, Optical image of a CrSBr bulk crystal with pump and probe pulse spatially separated by $d = 2 \mu m$. **b**, Transient reflectance spectra of the measurement shown in **a** ($d = 2 \mu m$) from which the incoherent electronic signal was subtracted. **c**-**e**, Probe-wavelength integrated STFT spectra at different pump-probe distances for the 24-GHz mode along the a axis (**c**) and along the b axis (**d**) and for the 34-GHz mode along the a axis (**e**). A moving time window of 0.15 ns is used for STFT. The same pump and probe laser conditions as in Fig. 1 are used and the sample temperature is 5 K. **f**, Spatially resolved MOKE imaging at a pump-probe delay time of 100 ps.

taking into account the small interlayer spin exchange in the vertical direction (c axis) and anisotropy exchange constants from fitting the magnetic resonance spectroscopy data in Fig. 2b. The dispersions along the in-plane Γ -X (a axis) and Γ -Y (b axis) directions are determined by the strong FM exchange interaction. Along the Γ -Z (c axis) direction, dispersion is essentially flat on the energy scale for Γ-X and Γ -Y and becomes visible only when we zoom-in by two orders of magnitude (Fig. 4b). The weak interlayer AFM couplings give rise to vertical bandwidths of only about 70 μeV, compared with about 40 meV in the in-plane directions. From the dispersions in Fig. 4a, we obtain group velocities (V_{α}) along the Γ -X and Γ -Y directions (Fig. 4c,d). There are two reasons why the observed propagating spin waves cannot be attributed to their intrinsic properties at sufficiently high momentum vectors (Q). First, owing to the negligible photon momentum, the optical pump-probe experiments can only probe magnons at the bottom of the dispersions, that is, near the Γ point. The spatial gradient may provide a parallel momentum vector of the order of about $1 \mu m^{-1}$, as dictated by the size of a diffraction-limited excitation. To realize $V_{\rm g}$ values of 1-3 km s⁻¹, the magnon dispersions dictate that intrinsic spin waves in the 2D plane (Fig. 4c,d) must possess Q values greater than 1 nm⁻¹, three orders of magnitude higher than what is experimentally possible. Second, the calculated V_{σ} values of the IP and OP modes are nearly identical in broad Q ranges along both the a and the b axes, contrary to the experimental ratio of $V_{g,OP}/V_{g,IP} = 3.0 \pm 0.4$ along the a axis and observation of only the IP mode along the b axis.

A well known mechanism for fast propagation of magnons at small momentum vectors is attributed to hybridization between magnon and acoustic phonons through magneto-elastic coupling^{33,34}. In this mechanism, the above-gap pump pulse creates thermally induced strain in magnetic materials and launches the hybridized magnon and phonon modes. Confirmation of this coupling mechanism comes from the short-time MOKE image (Fig. 3f) with the distinct quadrupolar shape, which is a signature of coupling of magnons to longitudinal acoustic phonons^{33,34}. Further support for this mechanism comes from peak splitting in the frequency domain (Supplementary Fig. 10), which can be directly attributed to hybridization and the resulting avoided crossing between the two modes. The two different group velocities

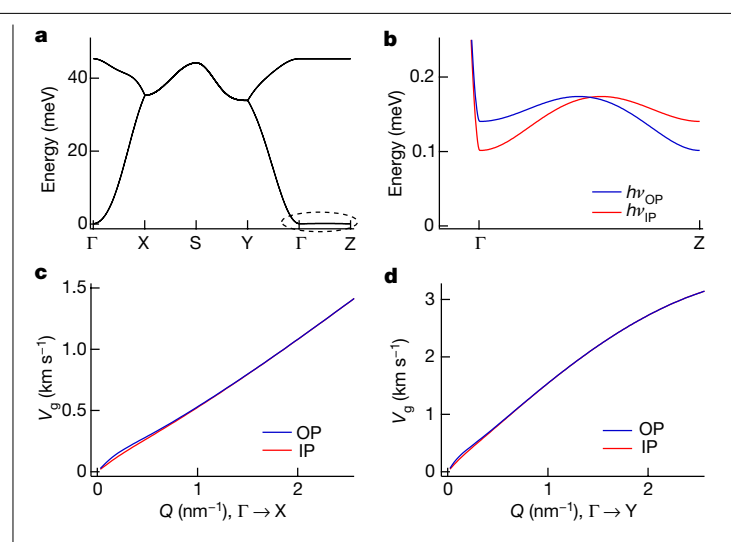


Fig. 4 | Magnon dispersions. a, Calculated magnon dispersions³². It is noted that the dispersions from the weak interlayer spin exchange in the Γ -Z direction (dashed oval) are nearly flat. \mathbf{b} , A magnified view of the Γ -Z direction showing the dispersions of in the out-of-phase (OP, blue) and in-phase (IP, red) modes. \mathbf{c} , \mathbf{d} , Momentum dependence of magnon group velocity along $\Gamma \rightarrow X$ (a axis; \mathbf{c}) and $\Gamma \rightarrow Y$ (b axis; **d**) directions.

presumably originate from crossing between two different acoustic phonon branches with different dispersions in momentum space.

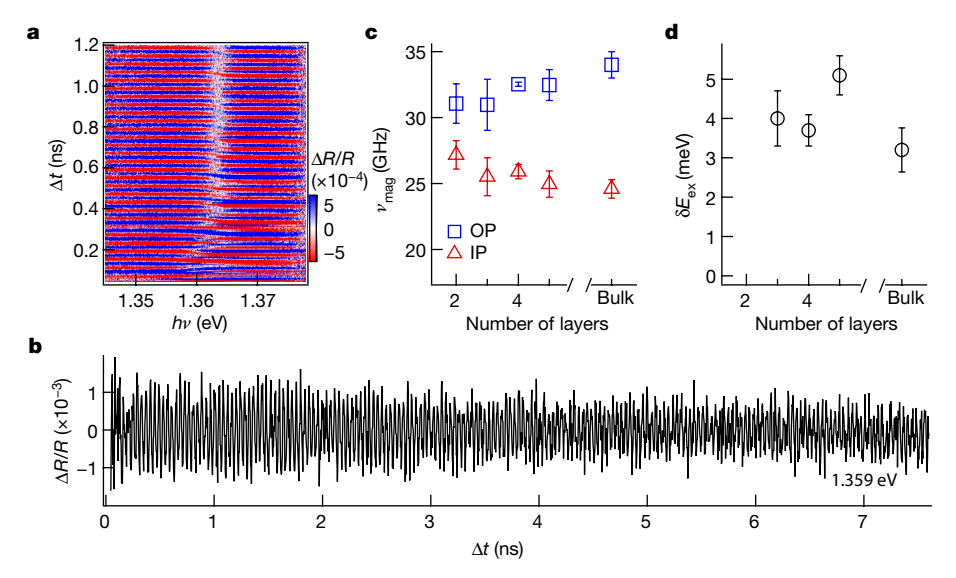
Coherent magnons down to the bilayer limit

The detection of coherent magnons in CrSBr from simple exciton sensing allows us to extend the measurements to the 2D limit on exfoliated flakes. It is noted that this approach cannot be used to probe the FM monolayer because it lacks interlayer exciton coupling²⁰. Similar to findings on the bulk crystal, the transient reflectance spectra from two layers (2L) to five layers (5L) (2L-5L) feature coherent oscillations attributed to spin waves. Figure 5a shows spectra for 5L CrSBr obtained under the same conditions as that in Fig. 1c. There is a clear π -phase flip in the oscillatory signal at the exciton peak of about 1.362 eV owing to the strong coupling of coherent magnons to the exciton. Figure 5b shows a line cut at $hv_2 = 1.359$ eV for the longest delay within our experimental limit, $\Delta t = 7.6$ ns. The coherent oscillation clearly persists beyond the experimental time window. A Lorentzian fit to its FFT (Supplementary Fig. 11) gives a full-width at half-maximum of 0.20 ± 0.02 GHz, corresponding to the coherence time, $\tau_{coh} = 5$ ns. Similar measurements for 2L-4L are shown in Supplementary Figs. 12-15. Supplementary Fig. 16 shows a quantitative analysis of coherence time from the 5L sample. These nanosecond coherence times are similar to those in the bulk crystal, $\tau_{\rm coh} = 2.5 - 5.0 \pm 0.5$ ns. It is noted that the measured $\tau_{\rm coh}$ and $\lambda_{\rm coh}$ represent lower bounds in the intrinsic coherence times and lengths, as the measurement with finite excitation pulse width, gradient in excitation profiles and inhomogeneity in sample environment introduces extrinsic decoherence.

Figure 5c summarizes the dependence of the spin-wave frequencies on the layer number. With increasing thickness, the frequency of the in-phase mode gradually decreases by about 10% (from 24.0 \pm 1.0 GHz to 24.6 ± 0.7 GHz), whereas that of the out-of-phase mode increases by about 10% (from 31 ± 1 GHz to 34 ± 1 GHz). Figure 5d plots the modulation in exciton energies, $\delta E_{\rm ex}$, by the coherent magnons for layer thicknesses ranging from 3L to thin bulk. The lower signal-to-noise ratio from the 2L sample prohibits a quantitative analysis of $\delta E_{\rm ex}$. Within experimental uncertainty, the magnon-exciton coupling energies from 3L to 5L (Supplementary Fig. 14) are the same as that from the bulk, $\delta E_{\rm ex} = 4.0 \pm 0.5$ meV. An attractive attribute of the coherent magnons approaching the 2D material limit is that they can have net magnetization for an odd (not even) number of layers. Having a net magnetization is essential for application as a quantum interconnect 15-17,35,36. In this regard, the sufficiently long coherence time and length may meet the needs for remote coupling of qubits or quantum emitters.

Summary and prospects

Our findings of exciton-coupled coherent magnons represent several key advances and may be applicable to vdW layered magnetic semiconductors in general, as long as the 2D excitons are of the Wannier type and interlayer electronic coupling is sufficiently influenced by interlayer magnetic order. The coupling of coherent magnons, living



 $Fig.\,5\,|\,Detection\,of\,coherent\,spin\,waves\,from\,excitonic\,transitions\,in$ CrSBr down to the 2D limit. a, Two-dimensional pseudo-colour plot of transient reflectance spectra from a 5L CrSBr flake as a function of pumpprobe delay (Δt) and probe photon energy (hv_2) at 5 K. **b**, Vertical cut of the spectra in **a** at $hv_2 = 1.359$ eV showing long-lived coherence. **c**, The frequency

of the in-phase (IP) and out-of-phase (OP) modes as a function of sample thickness. d, Magnitude of the exciton energy modulation with respect to the number of layers. The error bars are obtained from multiple samples and from the time average for $\delta E_{\rm ex}$ in each sample.

Article

in the sub-millielectronvolt energy range, to excitons living in the electronyolt region, can enable direct coupling between microwave photons and near-infrared to visible photons, potentially useful for quantum transduction. This coupled exciton-magnon also offers an opportunity to control the exciton properties of CrSBr by magnons, or vice versa, using optical or microwave cavities and electrostatic gating. In addition, the efficient exciton-magnon coupling opens the door to exciting applications, including integration with optoelectronics using on-chip light-emitting diodes and photodetectors. In this context, our observations of coherent magnons with excellent coherent properties down to the 2D bilayer limit suggest that CrSBr could be combined with other 2D materials through vdW heterojunctions, leading to novel device architectures and applications.

Online content

Any methods, additional references, Nature Research reporting summaries, source data, extended data, supplementary information, acknowledgements, peer review information; details of author contributions and competing interests; and statements of data and code availability are available at https://doi.org/10.1038/s41586-022-05024-1.

- Lee, J.-U. et al. Ising-type magnetic ordering in atomically thin FePS₃. Nano Lett. 16,
- 2. Gong, C. et al. Discovery of intrinsic ferromagnetism in two-dimensional van der Waals crystals. Nature 546, 265-269 (2017).
- Huang, B. et al. Layer-dependent ferromagnetism in a van der Waals crystal down to the monolayer limit. Nature 546, 270-273 (2017).
- Gibertini, M., Koperski, M., Morpurgo, A. F. & Novoselov, K. S. Magnetic 2D materials and heterostructures. Nat. Nanotechnol. 14, 408-419 (2019).
- Gong, C. & Zhang, X. Two-dimensional magnetic crystals and emergent heterostructure devices, Science 363, eaay 4450 (2019)
- Mak, K. F., Shan, J. & Ralph, D. C. Probing and controlling magnetic states in 2D layered magnetic materials. Nat. Rev. Phys. 1, 646-661 (2019).
- 7. Zhong, D. et al. Layer-resolved magnetic proximity effect in van der Waals heterostructures, Nat. Nanotechnol, 15, 187-192 (2020).
- Tang, C., Zhang, Z., Lai, S., Tan, Q. & Gao, W. Magnetic proximity effect in graphene/CrBr₃ van der Waals heterostructures. Adv. Mater. 32, 1908498 (2020).
- 9. Tong, Q., Liu, F., Xiao, J. & Yao, W. Skyrmions in the moiré of van der Waals 2D magnets. Nano Lett. 18, 7194-7199 (2018)
- Huang, B. et al. Emergent phenomena and proximity effects in two-dimensional magnets and heterostructures. Nat. Mater. 19, 1276-1289 (2020).
- Wang, C., Gao, Y., Lv, H., Xu, X. & Xiao, D. Stacking domain wall magnons in twisted van der Waals magnets. Phys. Rev. Lett. 125, 247201 (2020).
- Zhang, X.-X. et al. Gate-tunable spin waves in antiferromagnetic atomic bilayers. Nat. Mater. 19, 838-842 (2020).

- Chumak, A. V., Vasyuchka, V. I., Serga, A. A. & Hillebrands, B. Magnon spintronics. Nat. Phys. 11, 453-461 (2015)
- Kruglyak, V. V., Demokritov, S. O. & Grundler, D. Magnonics. J. Phys. D 43, 264001 (2010).
- Li, Y. et al. Hybrid magnonics: physics, circuits, and applications for coherent information processing. J. Appl. Phys. 128, 130902 (2020).
- Lachance-Quirion, D., Tabuchi, Y., Gloppe, A., Usami, K. & Nakamura, Y. Hybrid quantum systems based on magnonics. Appl. Phys. Express 12, 70101 (2019).
- Awschalom, D. D. et al. Quantum engineering with hybrid magnonic systems and materials. IEEE Trans. Quantum Eng. 2, 1-36 (2021).
- Telford, E. J. et al. Layered antiferromagnetism induces large negative magnetoresistance in the van der Waals semiconductor CrSBr. Adv. Mater. 32, 2003240 (2020).
- Lee, K. et al. Magnetic order and symmetry in the 2D semiconductor CrSBr. Nano Lett. 21. 3511-3517 (2021).
- Wilson, N. P. et al. Interlayer electronic coupling on demand in a 2D magnetic semiconductor, Nat. Mater. 20, 1657-1662 (2021).
- 21 Kang, S. et al. Coherent many-body exciton in van der Waals antiferromagnet NiPS. Nature 583 785-789 (2020)
- Hwangbo, K. et al. Highly anisotropic excitons and multiple phonon bound states in a van der Waals antiferromagnetic insulator. Nat. Nanotechnol. 16, 655-660 (2021).
- 23. Wang, X, et al. Spin-induced linear polarization of photoluminescence in antiferromagnetic van der Waals crystals. Nat. Mater. 20, 964-970 (2021)
- Mak, K., Lee, C., Hone, J., Shan, J. & Heinz, T. Atomically thin MoS₂: a new direct-gap semiconductor. Phys. Rev. Lett. 105, 136805 (2010).
- 25. Splendiani, A. et al. Emerging photoluminescence in monolayer MoS₂. Nano Lett. 10, 1271-1275 (2010).
- Němec, P., Fiebig, M., Kampfrath, T. & Kimel, A. V. Antiferromagnetic opto-spintronics. Nat. Phys. 14, 229-241 (2018).
- Kumar, A. T. N., Rosca, F., Widom, A. & Champion, P. M. Investigations of amplitude and phase excitation profiles in femtosecond coherence spectroscopy, J. Chem. Phys. 114. 701-724 (2001).
- Lüer, L. et al. Coherent phonon dynamics in semiconducting carbon nanotubes: a quantitative study of electron-phonon coupling. Phys. Rev. Lett. 102, 127401 (2009)
- MacNeill, D. et al. Gigahertz frequency antiferromagnetic resonance and strong magnonmagnon coupling in the layered crystal CrCl₃. Phys. Rev. Lett. 123, 47204 (2019)
- Shen, X, et al. Multi-domain ferromagnetic resonance in magnetic van der Waals crystals Crl₃ and CrBr3. J. Magn. Magn. Mater. 528, 167772 (2021).
- Gurevich, A. G. & Melkov, G. A. Magnetization Oscillations and Waves (CRC, 1996).
- Scheie, A., Ziebel, M., Chica, D. G., Bae, Y. J., Wang, X., Kolesnikov, A. I., Zhu, X., Roy, X. Spin Waves and Magnetic Exchange Hamiltonian in CrSBr. Adv. Sci. https://doi.org/10.1002/ advs.202202467 (2022)
- Shen, K. & Bauer, G. E. W. Theory of spin and lattice wave dynamics excited by focused laser pulses. J. Phys. D 51, 224008 (2018).
- Ogawa, N. et al. Photodrive of magnetic bubbles via magnetoelastic waves. Proc. Natl Acad. Sci. USA 112, 8977-8981 (2015).
- Dany, L.-Q. et al. Entanglement-based single-shot detection of a single magnon with a superconducting qubit. Science 367, 425-428 (2020).
- Yutaka, T. et al. Coherent coupling between a ferromagnetic magnon and a superconducting qubit. Science 349, 405-408 (2015).

Publisher's note Springer Nature remains neutral with regard to jurisdictional claims in published maps and institutional affiliations

© The Author(s), under exclusive licence to Springer Nature Limited 2022

Methods

CrSBr synthesis and sample preparation

The following reagents were used as received unless otherwise stated: chromium powder (99.94%, -200 mesh, Alfa Aesar), sulfur pieces (99.995%, Alfa Aesar) and bromine (99.99%, Aldrich). To synthesize chromium bromide (CrBr₃), chromium (1.78 g, 34.2 mmol) and bromine (8.41 g, 105 mmol) were loaded into a bent, 19-mm outer diameter (OD), 14-mm inner diamaeter (ID) fused silica tube. The tube was evacuated to a pressure of about 30 mtorr and flame sealed while the bottom was submerged in liquid nitrogen. The end of the tube containing chromium was heated at 1,000 °C for 3 d while the other end outside the furnace was maintained below 50 °C to prevent over pressurizing the tube. Caution: Heating the entire tube above 120 °C with significant excess of bromine can result in explosion of the tube. To synthesize CrSBr, in a typical reaction, chromium (0.189 g, 3.63 mmol), sulfur (0.196 g, 6.11 mmol) and chromium tribromide (0.720 g, 2.47 mmol) were loaded into a 12.7-mm OD, 10.5-mm ID fused silica tube. The tube was evacuated to a pressure of about 30 mtorr and flame sealed to a length of 12 cm. The tube was placed into a computer-controlled, two-zone, tube furnace. The source side was heated to 550 °C in 6 h, allowed to soak for 12 h, heated to 930 °C in 12 h, allowed to soak for 84 h, then water quenched. The sink side was heated to 570 °C in 6 h, allowed to soak for 12 h, heated to 970 °C in 12 h, allowed to soak for 24 h, cooled to 850 °C in 12 h, allowed to soak for 48 h, then water quenched. Caution: Proper personal protective equipment should be worn when water quenching tubes, including face shield, thick heat-resistant gloves and a fire-resistant lab coat. The crystals were cleaned by soaking in acetonitrile for 1 h, followed by soaking in deionized water for 16-24 h at 70 °C. After soaking, the crystals were thoroughly rinsed with deionized water and acetone.

Following synthesis, bulk crystals were mechanically exfoliated onto a silicon wafer with a 90-nm-thick silicon dioxide (SiO_2) layer passivated by 1-dodecanol inside a glove box ^{37,38}. Sample optical and atomic force microscope images of the CrSBr flakes were taken to identify the number of layers as shown in Supplementary Figs. 17 and 18.

Transient reflectance spectroscopy at a fixed magnetic field

To enhance excitonic sensing of the spin waves, we apply an external magnetic field ($B_0 = 0.2 \text{ T}$) along the c axis to tilt the spins. Although the oscillations are present at zero magnetic field (Supplementary Fig. 2), the amplitude is significantly smaller. In the AFM phase, a change to $E_{\rm ex}$ owing to interlayer hybridization is $\Delta E_{\rm ex} \propto \cos(\theta/2)^2$, with $\theta = (\pi - \alpha_0) \pm \alpha$, where α_0 is the reduction of θ caused by B_0 and α is the time-dependent modulation of θ by the coherent spin wave. As $dE_{ex}/d\theta \propto \sin(\alpha_0 + \alpha)$, having a non-zero α_0 enhances the oscillatory signal, which we measure as oscillation in $E_{\rm ex}$. We excite CrSBr by $hv_1 = 1.7$ eV and measure the change in reflectance at a variable time delay (Δt) by a broadband probe $(hv_2 = 1.3 - 1.4 \text{ eV}; \text{Supplementary Fig. 19})$ to obtain transient reflectance, $\Delta R/R$, where ΔR is the differential reflectance with and without the pump and R is reflectance without the pump. A detailed description of all optical measurements is shown in the Supplementary Section 11. This energy region probes the excitonic transitions38, as shown by the static reflectance spectrum in Fig. 1b. Each $\Delta R/R$ spectrum with above-gap photoexcitation features coherent oscillations on top of an incoherent background (Supplementary Fig. 20). We isolate the pure oscillatory response by subtracting the incoherent signal attributed to electronic excitations for a thin-bulk CrSBr at T = 5 K and d = 0 μ m (Fig. 1c). We choose the pump laser power in the linear electronic excitation region with sufficient oscillatory amplitude (Supplementary Fig. 21). At low power, the magnon FFT amplitude linearly increases with the pump power but eventually plateaus. The pump power has a minimal effect on magnon frequency.

Coherent magnon launching mechanism

The results presented above on exciton-coupled coherent magnons focus on how the latter modulates the former. The coherent magnons

are launched by above-gap excitation, with the excitation polarization dependences (Supplementary Fig. 21) in qualitative agreement with the optical anisotropy of the excitonic transitions 38 . Excitonic transitions in the fully spin-polarized band structure 38 can modify the spin-exchange interactions and perturb the magnetic order on ultrafast timescales 39 , thus launching the magnon wavepacket. However, the initial electronic transition can also result in secondary excitations, particularly coherent phonons, that may launch coherent magnons via the magneto-elastic coupling 40,41 , which is probably responsible for the in-plane propagating magnons in Fig. 3. In principle, the primary electronic and excitonic, and the secondary magneto-elastic launching mechanisms may be distinguished from the delayed rise of coherent magnons in the latter, but the low magnon frequency and limited time resolution prohibit such a distinction in our experiment. This issue deserves future experiments on shorter timescales and at higher time resolutions.

Magnetic resonance spectroscopy

We collected magnetic resonance spectra using a broadband co-planar waveguide method in a Quantum Design Physical Property Measurement system at variable temperatures and variable magnetic fields. An exfoliated CrSBr bulk sample (5 mm by 2 mm) is mounted on a co-planar waveguide where an a.c. current provides a small oscillating Oersted field that drives the magnetization into a small-angle precession. At the resonance condition, the amplitude of the precession is maximized. An external d.c. magnetic field is applied perpendicular to the sample plane. The frequency of the a.c. field is fixed while the d.c. magnetic field is swept from 3 T to zero with a step size of 0.02 T. Both the transmission and reflection spectra are collected using a vector network analyser. The real part of the transmission port is plotted with respect to the swept magnetic field (Supplementary Fig. 6). A linear combination of symmetric and antisymmetric Lorentzian functions is used to extract the peak position of the resonance peaks (Supplementary Fig. 6).

We then model the field dependence of the modes by minimizing the spin structure with various values of the external magnetic field and recalculating the Q = 0 modes using the SpinW version 3.1 software package, which is described below, as well as the macrospin model using the Landau–Lifshitz (LL) equations (Supplementary Section 14)⁴². As the interplane exchange is unknown, we model the field dependence using many different net interlayer-exchange J_{int} values, adjusting single-ion anisotropy terms, A_z and A_y to produce the observed zero-field magnon energies (Supplementary Fig. 22). We find that interplane exchange energy below 0.04 meV is required to have both magnon modes initially decrease energy with the magnetic field, with a more realistic value closer to 0.02 meV. It is noted that getting the LSWT calculated transition field—the kink in magnon energy—to match the experiment requires an $adjusting \, of \, the \, g \, value \, to \, less \, than \, 2, similar \, to \, the \, adjust ment \, required$ for the gyromagnetic ratio in the LL equations. Thus, by having observed the energy and field dependence of the Q = 0 magnon modes, we can place an upper bound on the CrSBr interplane exchange interactions: three orders of magnitude weaker than the intraplanar exchange³².

Linear spin-wave theory

As a semiclassical alternative approach to the classical LL equations, we also calculated the magnon modes using LSWT. As the relevant exchange interactions for the Q=0 modes observed here do not depend on the in-plane exchange interactions, we can model the system as a one-dimensional AFM spin chain with anisotropy. We write the Hamiltonian as

$$H = \sum_{i} J_{\text{int}} \, \hat{S}_{i} \cdot \hat{S}_{i+1} + A_{x} \, \hat{S}_{x}^{2} + A_{z} \, \hat{S}_{z}^{2}$$

where \hat{S} are spin operators for spin i and i+1, J_{int} is the net interlayer-exchange interaction, and A_x and A_z are single-ion anisotropy terms. Here we assume that A_x and A_z are both positive and A_y is zero such that

Article

the easy axis is in the b direction. Solving this equation for the magnon modes using the Holstein–Primakoff formalism⁴³ gives the formulae in the main text for the two low-energy modes. It is noted that these modes are the acoustic intraplane magnon mode, split by the presence of interplane exchange and magnetic anisotropy. It is also noted that the presence of an intermediate axis is crucial to the observation of two modes at zero applied magnetic field: in a single easy-axis case, $A_z = A_x$, the two B = 0 modes are degenerate.

We quantitatively analyse the B_0 dependence of the magnon frequencies using the Heisenberg spin Hamiltonian and fitting the magnetic resonance spectroscopy data using LSWT³², with the fitting details shown in Supplementary Fig. 22 (Supplementary Section 13). The triaxial anisotropy in spin-exchange interaction and interlayer-exchange interaction in CrSBr results in two non-degenerate magnon modes. The LSWT analysis gives the in-phase mode at frequency $v_{\rm IP} = 2S\sqrt{A_xA_z + A_xJ_{\rm int}}$ and the out-of-phase mode at frequency $v_{\rm OP} = 2S\sqrt{A_xA_z + A_zJ_{\rm int}}$ where S is the total spin quantum number. The A_x , A_z and $J_{\rm int}$ values from LSWT fits (solid curves in Fig. 2b) are 14 μ eV, 58 μ eV and 6 μ eV, respectively. The fits give magnon frequencies at $B_0 = 0.2$ T (external field used in Fig. 1) of $v_{\rm IP} = 24.4$ GHz and $v_{\rm OP} = 33.8$ GHz, in good agreement with those measured from exciton sensing. Similar agreement with experimental results is also achieved in analysis based on the classical LL equations³¹, with the spin configuration shown in Supplementary Fig. 23 (Supplementary Section 14).

Data availability

The data that support the plots within this paper are available from the corresponding author upon reasonable request. Source data are provided with this paper.

- Lee, K. et al. Magnetic order and symmetry in the 2D semiconductor CrSBr. Nano Lett. 21, 3511–3517 (2021).
- Wilson, N. P. et al. Interlayer electronic coupling on demand in a 2D magnetic semiconductor. Nat. Mater. 20, 1657–1662 (2021).
- Němec, P., Fiebig, M., Kampfrath, T. & Kimel, A. V. Antiferromagnetic opto-spintronics. Nat. Phys. 14, 229–241 (2018).

- Shen, K. & Bauer, G. E. W. Laser-induced spatiotemporal dynamics of magnetic films. Phys. Rev. Lett. 115. 197201 (2015).
- Ogawa, N. et al. Photodrive of magnetic bubbles via magnetoelastic waves. Proc. Natl Acad. Sci. USA 112, 8977–8981 (2015).
- Toth, S. & Lake, B. Linear spin wave theory for single-Q incommensurate magnetic structures. J. Phys. Condens. Matter 27, 166002 (2015).
- Holstein, T. & Primakoff, H. Field dependence of the intrinsic domain magnetization of a ferromagnet. Phys. Rev. 58, 1098–1113 (1940).

Acknowledgements The spectroscopic and imaging work was supported by the Materials Science and Engineering Research Center (MRSEC) through NSF grant DMR-2011738, with partial support for experimental apparatus by the Vannevar Bush Faculty Fellowship through the Office of Naval Research grant number NO0014-18-1-2080. The synthesis of the CrSBr crystals was supported as part of Programmable Quantum Materials, an Energy Frontier Research Center funded by the US Department of Energy (DOE), Office of Science, Basic Energy Sciences (BES), under award DE-SC0019443. The magnetic resonance spectroscopy work was supported by the Air Force Office of Scientific Research under grant FA9550-19-1-0307. The magnetic-field-dependent experiment in Fig. 2c was supported by the Department of Energy, Basic Energy Sciences, Materials Sciences and Engineering Division (DE-SC0012509). The vibrating sample magnetometry was purchased with financial support from the NSF through a supplement to award DMR-1751949. This research used resources at the Spallation Neutron Source, a DOE Office of Science User Facility operated by the Oak Ridge National Laboratory. This research was supported by an appointment to the Intelligence Community Postdoctoral Research Fellowship Program at University of Washington administered by Oak Ridge Institute for Science and Education (ORISE) through an interagency agreement between the US Department of Energy and the Office of the Director of National Intelligence (ODNI). We are grateful to K. Lee, T. Handa and Y. Dai for providing help and discussions

Author contributions X.Z. and Y.J.B. conceived this work. Y.J.B. carried out all optical measurements at fixed magnetic fields with assistance from J.W., Y.B. and M.D. Bulk crystals were synthesized and characterized by D.G.C. and M.E.Z. under the supervision of X.R. and C.R.D. The magnetic resonance measurements were carried out by Y.J.B., J.X. and H.R. under the supervision of A.D.K. The magnetic-field-dependent optical measurements were performed by G.M.D. and J.C. under the supervision of X.X. Theoretical analysis was performed by Y.J.B. and A.S. X.Z. supervised the project. The manuscript was prepared by Y.J.B. and X.Z. in consultation with all other authors. All authors read and commented on the manuscript.

Competing interests The authors declare no competing interests.

Additional information

Supplementary information The online version contains supplementary material available at https://doi.org/10.1038/s41586-022-05024-1.

Correspondence and requests for materials should be addressed to Xiaoyang Zhu.

Peer review information Nature thanks Jun-Bo Han and the other, anonymous, reviewer(s) for their contribution to the peer review of this work.

Reprints and permissions information is available at http://www.nature.com/reprints.